Segmentation-Driven Image Registration-Application to 4D DCE-MRI Recordings of the Moving Kidneys

Erlend Hodneland, Erik A. Hanson, Arvid Lundervold, Jan Modersitzki, Eli Eikefjord, and Antonella Z. Munthe-Kaas

***Abstract*— Dynamic contrast enhanced magnetic resonance imaging (DCE-MRI) of the kidneys requires proper motion correction and segmentation to enable an estimation of glomerular filtration rate through pharmacokinetic modeling. Traditionally, co-registration, segmentation, and pharmacokinetic modeling have been applied sequentially as separate processing steps. In this paper, a combined 4D model for simultaneous registration and segmentation of the whole kidney is presented. To demonstrate the model in numerical experiments, we used normalized gradients as data term in the registration and a Mahalanobis distance from the time courses of the segmented regions to a training set for supervised segmentation. By applying this framework to an input consisting of 4D image time series, we conduct simultaneous motion correction and two-region segmentation into kidney and background. The potential of the new approach is demonstrated on real DCE-MRI data from ten healthy volunteers.**

***Index Terms*— Image registration, image segmentation, active contours, DCE-MRI, Mahalanobis distance, GFR.**

I. Introduction

THE Glomerular Filtration Rate (GFR) is an important parameter in the assessment of kidney dysfunction and disease [53]. It is a measure of the volume of filtered fluid per unit time from the blood pool in the glomerular capillaries to the tubular space in Bowman's capsule. A schematic overview of a kidney is depicted in Fig. 1, showing cortex, medulla and the pelvis. Low values of GFR are associated with kidney dysfunction and renal disease. Serum creatinine is the most commonly used measure for GFR. Other and more accurate filtration markers are Iohexol (serum clearance) and Inulin (urinary clearance) for the total kidney GFR estimation. However, none of these approaches permit voxel-wise assessment within the kidney, or a differentiation of function (split-function) between left and right kidney. On the other hand, MR renography, based on intravenous injection of a contrast agent and dynamic scanning over time using a fast T1-weighted pulse sequence, offers the possibility to obtain voxel-wise measurements of kidney function. In this respect, dynamic contrast-enhanced magnetic resonance imaging (DCE-MRI) is an in vivo imaging method for measurement of physiological parameters like perfusion, transfer rates, permeability-surface products, and capillary leakage in normal and abnormal tissue in a wide range of organs and disease processes. However, the DCE-MRI approach for measurements of local or total renal GFR is not yet available in clinical routine, due to lack of accuracy and reproducibility [31]. This is probably attributable to noise and MR artifacts in the acquisitions, organ motion, inaccurate segmentation of the kidney compartments, inaccuracy in the mapping of signal into Gadolinium concentrations, and shortcoming and instability of the applied pharmacokinetic

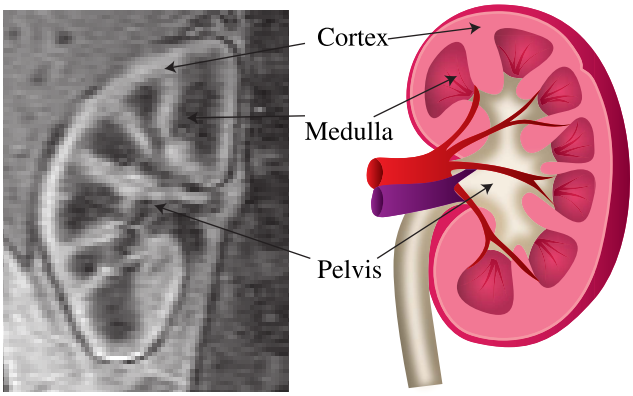

Fig. 1. The human kidney with anatomical compartments *cortex*, *medulla* and *pelvis*. The filtration takes place in the cortical and juxta-medullary nephrons of the kidney, regions for which voxel-wise GFR can be estimated. **Left panel**: Coronal section and time frame from a DCE-MRI examination showing the wash-in of contrast agent into the cortical region. **Right panel**: Anatomical sketch of the kidney showing the different renal compartments as well as the renal artery inlet (red), the renal vein outlet (blue), and the urinary outlet (*ureter*). Courtesy to Silje Søviknes.

Manuscript received December 9, 2013; revised March 11, 2014; accepted March 16, 2014. Date of publication April 1, 2014; date of current version April 22, 2014. The associate editor coordinating the review of this manuscript and approving it for publication was Prof. Jeffrey A. Fessler.

E. Hodneland is with the Department of Biomedicine, University of Bergen, Bergen 5020, Norway (e-mail: erlend.hodneland@biomed.uib.no).

E. A. Hanson and A. Z. Munthe-Kaas are with the Department of Mathematics, University of Bergen, Bergen 5020, Norway (e-mail: erik.hanson@math.uib.no; antonella.zanna@math.uib.no).

A. Lundervold is with the Department of Biomedicine, University of Bergen, Bergen 5020, Norway, and also with the Department of Radiology, Haukeland University Hospital, Bergen 5021, Norway (e-mail: arvid.lundervold@biomed.uib.no).

J. Modersitzki is with the Institute of Mathematics and Image Computing, University of Lübeck, Lübeck 23562, Germany (e-mail: jmodersitzki@gmail.com).

E. Eikefjord is with the Department of Radiology, Haukeland University Hospital, Bergen 5021, Norway (e-mail: eli.nina.eikefjord@helse-bergen.no).

Color versions of one or more of the figures in this paper are available online at http://ieeexplore.ieee.org.

Digital Object Identifier 10.1109/TIP.2014.2315155

This work is licensed under a Creative Commons Attribution 3.0 License. For more information, see creativecommons.org/licenses/by/3.0/

compartment models. Hence, the reliability and reproducibility of the obtained GFR values can become unacceptably low if the recorded data are not properly processed. Despite these obstacles and challenges, DCE-MRI has a great potential to become an important tool in the diagnosis, therapy planning, and follow-up of patients with renal artery stenosis, renal parenchymal disease, polycystic kidney disease, and kidney graft rejection [53].

In an ideal setting, voxel-based GFR measurements from DCE-MRI acquisitions would enable a tissue and site specific analysis of kidney function. In practice, however, voxel-based measurements are corrupted by lack of reliability in at least three major processing steps: (i) registration (motion correction of organ motion), (ii) segmentation (identification of tissue compartments), and (iii) the establishment of a pharmacokinetic model. As a first step towards an integrated model, we here attack the first two processing steps simultaneously, registration and segmentation.

1) Registration: Proper registration is a critical step in the processing chain, as uncorrected voxel displacements will corrupt the voxel time courses. The motion artefacts are caused by respiratory motion, intestinal peristalsis, cardiac pulsations, or patient movement during data collection [32], [48]. In this way, GFR estimates can become strongly biased or even invalidated [55]. To perform motion correction, affine registration has been used by several authors [2], [9]. Affine registration can also be used as an initialization step to a supplementary deformable registration. Clearly, due to respiration there is a significant local affine motion component directed along the head-to-feat axis, as modelled in [40] and also observed in our experiments (cf. Section IV-E.3). Still, there is also a deformable motion component due to the elastic properties of the kidney, deforming along with local geometric restrictions in the proximate surroundings.

The model presented in this work is rather general and the choice of data terms is basically open and not a topic for discussion here. Still, an optimal data term is necessary in order to obtain the best possible registration. In the literature, deformable image registration of DCE-MRI time series for estimation of GFR has mainly been accomplished using (normalized) mutual information (N)MI [48], [52], [56], which is regarded as a method-of-choice in multi modal registration [28], [49]. Normalized mutual information or mutual information has also been applied in several recent methodological papers for co-registration of DCE-MRI time series [27], [37], [48], although an optimal method has not yet been settled [45]. Normally, the images contain durable edge information between various tissue types, and also within the kidney after the arrival of contrast agent. This phenomenon favours the use of a gradient dependent cost functional for registration. In recent work [14], [24] it was shown that normalized gradient fields (NGF) was a viable alternative to MI for the registration of DCE-MRI images. In this work, we therefore incorporate a version of NGF [21], [35] as data term for the registration task.

2) Segmentation: The task of *segmenting* the kidney in DCE-MRI recordings has taken several approaches [57]. Manual delineation performed by an expert is potentially accurate, but also highly subjective and time consuming in contrast to automated methods [41]. Automated segmentation methods employing k-means clustering [56] and k-nearest neighbor classification [25] have been proposed. For these methods the signal intensities in time are used as a high-dimensional feature vector in each voxel. The advantage of these approaches is that the classification of a tissue voxel is based on the actual tissue response to the bolus wash-in and wash-out. Alternatively, active contours [1] and related methods employing region and boundary properties in combination with shape constraints [3] have been used. In this work, we apply the temporal tissue response and minimal boundary length as shape information for the segmentation.

3) Compartment Modeling: Renal filtration, mainly taking place in the renal cortex, can be estimated using compartment models within a defined segmentation of the kidney [4], [45], [46]. The compartment time series are then fed into the chosen pharmacokinetic model, producing voxel-wise parameters that best match the data. Compartment-wise parameters can be obtained summing up the voxel-wise contributions over the whole compartment. A valid estimation of GFR thus depends on a successful registration and segmentation, which are the critical steps in the processing chain.

4) Combined Registation and Segmentation: A significant portion of the disagreements between DCE-MRI estimated and iohexol-estimated GFR can originate from at least three of the above mentioned processing steps that are executed separately [31]: registration, segmentation, and compartment modeling. Errors occurring in one step are propagated to the next, not being adjusted or compensated for since the steps are essentially uncoupled. This is the major motivation for our proposed method, a combined registration and segmentation where the segmentation has a feedback term in the registration, thus assisting towards a more consistent alignment of time points. Several works in other reseach areas report that a combined segmentation and registration improves the overall performance compared to a sequential processing [15], [17], [51].

Yezzi et al. [51] introduced the idea of coupling the registration and segmentation in a framework of active contours. Segmentations of the input and target image combined with a joint affine registration were used to improve both the registration and segmentation accuracy of 2D images. Their method was not suited to incorporate non-affine deformations in the registration part due to the linearity. In numerous publications [15], [17], [20], [36], [42], an inital segmentation is assumed, and this prior information is used to guide a combined registration and segmentation of either the input or the reference image, depending on the application. Thereby, the input and reference images are matched along the curve enclosing the segmented region and the rest of the image is deformed according to the regularization of the deformation field. In some of these publications an additional image similarity measure was applied, usually the sum-of-squared differences (SSD) [15], [42]. A combined segmentation/registration expressed in a segmentation framework is particularly advantageous in the presence of an atlas ground truth. Iterative, sequential approaches

were also used in [43] and [54] for a serial registration and segmentation.

In our proposed model for registration/segmentation, we explore the idea from Yezzi et al. [51] and suggest to execute the registration jointly with the segmentation, and not iteratively or sequentially as in [43] and [54]. We define the optimization problem directly within a common variational framework, solving for both the registration and segmentation simultaneously, and coupling the registration/segmentation via the segmentation term. Thus, the registration becomes directly segmentation-driven within the cost functional, favoring a displacement field consistent with an improved spatio-temporal separation of various tissue or compartments. Hence, we assume that the temporal signal response is similar within the same tissue or compartment type, or pathophysiological condition. Unlike the approach in [51] we also include a classical image registration data term in order to incorporate image information away from the segmentation boundaries. As a major difference to the methods depending on a prior segmentation, we use a time-normalized, continuous Mahalanobis distance to a training set.

To the best of our knowledge, our described application is novel and represents a new approach to quantitative MRI renography. We claim to represent the first work exploring the Mahalanobis distance and a training set for a 4D joint registration and segmentation, in particular for artifact and noise loaded DCE-MRI images. Thus, this work represents a major step towards an integrated model with combined registration, segmentation and compartment modeling, and can further be extended towards model-driven deformable registration in DCE-MRI processing [2], [9], [22].

In the following, we first describe our combined model for registration and segmentation. Then, we show experimental results from ten different kidney DCE-MRI time series recorded in healthy volunteers, and finally, we discuss the proposed method and future perspectives.

II. Methods

A. Mathematical Framework and Problem Formulation

The DCE-MRI times series are 4D data sets mapping from time and space into positive and real intensity scalar values $f : \mathbb{R}^3 \times \mathbb{R} \to \mathbb{R}$. Denote the the whole time series as the input image $f(x,t)$ for Lagrangian coordinates x. The reference image f_r can be any selected 3D image in the discrete time series, $f_r(x) = f(x,t_r), t_r \in T_d$, where $T_d = \{t_1, t_2, \ldots, t_n\}$ is the set of discrete time points for image acquisition, $T_d \subset T, T = \{t \in \mathbb{R} : t_1 \leq t \leq t_n\}$. A single selected time frame after bolus arrivel was chosen as the reference image.

For deformable registration, the aim is to find a voxelwise deformation field $u : \mathbb{R}^3 \times \mathbb{R} \to \mathbb{R}^3$ such that the time series is optimally aligned for all voxels along all time points. The registration of DCE-MRI times series is a 4D (space and time) registration problem with respect to data, but a 3D optimization problem. The reason for this discrepancy is the assumption that the data are sampled on discrete time points, hence there should be no transport of information along the time axis. All motion artifacts are therefore assumed to be spatial. Following the approach of [35], the registration of frame $f(x,t)$ to the reference can be phrased as an optimization problem. The overall goal is to find a minimizer u of a cost functional J where

$$J(u) = \int_T \int_\Omega D(f(x+u,t),\, f_r(x)) + R(u) dx dt \qquad (1)$$

and where D is the data term and R is the regularization [34]. The data term attempts to align the input image with the target image by maximizing a similarity measure between those, for instance mutual information, normalized gradients, cross correlation or least squares [34]. Registration is an ill-posed problem and the regularization terms are required to ensure a sufficiently smooth deformation field by penalizing spatially large and strongly varying deformations [18]. The minimization of (1) produces as output a deformation field maximizing the similarity measure of choice.

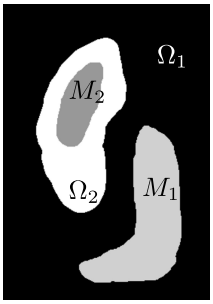

Fig. 2. Schematically visualized segmented regions Ω_1 and Ω_2 representing background and kidney, respectively. Manually given 2D training set regions M_1 and M_2 are also indicated, which are used to create a training set of typical time courses for each partition Ω_i, guiding the segmentation towards the desired solution. Each training set region M_i must be placed well inside the expected Ω_i with a minimum distance to the region boundary of $u_{\max}$ such that $u_{\max} = \max_{\partial M_i} |u|$. After segmentation we observe that $M_i \subset \Omega_i$, although this is not mathematically guaranteed.

The overall aim of the analysis is to compute GFR values within the kidney, and a segmentation of the kidney is therefore useful to have. In this respect, we add a minimization term for a two-region segmentation, with the potential to distinguish kidney from non-kidney tissue using temporal image information as features. A spatial map $d(x, M_i)$ is defined, reflecting the deviation between the time series $f(x,t)$ and the time series within a training set region $M_i, i = 1, 2$. A voxel x will be assigned to region Ω_i such that the cost $d(x, M_i)$ will be the smallest, i.e. $i = argmin_j(d(x, M_j))$ for $j = 1, 2$. An example of sets M_i associated with the partitioning Ω_1 and Ω_2 is displayed in Fig. 2. For such segmentation task we consider a two-region Potts model [39] for segmentation of the image domain Ω,

$$\begin{aligned} &\min_{\Omega_1,\Omega_2} S(\Omega_1, \Omega_2), \\ &S(\Omega_1, \Omega_2) = \int_{\Omega_1} d(x, M_1)^2 dx + \int_{\Omega_2} d(x, M_2)^2 dx + \alpha|\Gamma| \\ &\text{such that } \overline{\Omega}_1 \cup \overline{\Omega}_2 = \overline{\Omega}, \quad \Omega_1 \cap \Omega_2 = \emptyset \end{aligned} \qquad (2)$$

The length of the common boundary of Ω_1 and Ω_2 is denoted $|\Gamma| = |\partial\Omega_1 \cap \partial\Omega_2|$. Due to the boundary term, this model favours segmentation with 'tight' boundaries and little

oscillations [39]. The weight of the constraint is controlled by the parameter $\alpha \geq 0$. A higher value of α will reduce the curve length $|\Gamma|$ and create a smoother boundary between Ω_1 and Ω_2. The construction of (2) ensures no vacuum or overlap between the segmented regions.

We now combine equations (1) and (2) into a single cost functional for minimization, $J(u) + S(\Omega_1, \Omega_2)$. In order to obtain a segmentation driven registration we also make the replacement

$$d(x, M_i) \rightarrow d(x + u, M_i), \tag{3}$$

thus coupling the registration with the segmentation via the deformation field u. A special property of this model is that the registration will be driven not only by the data and regularization term as in (1), but also from the segmentation, thus favouring displacements maximizing the similarity between time curves within the same segment. This is justified since functionally related biological tissue is likely to exhibit similar intensity profiles.

B. The Unconstrained Problem

The unconstrained optimization problem is achieved by using a level set method for the segmentation and by introducing binary indicator functions for the user-defined segmentation regions. Let $\phi : \mathbb{R}^3 \rightarrow \mathbb{R}$ be a level set function, as in the Chan-Vese method [10]. The segments, which are separated by Γ, are represented by a zero-thresholding of ϕ, $\Omega_1 = \{x : \phi(x) > 0\}$, $\Omega_2 = \{x : \phi(x) < 0\}$. Thus, there is no overlap between the regions, and every $x \in \Omega$ belongs to a segment $\Omega_i, i = 1, 2$ or to their common boundary, as required. An unconstrained formulation of the segmentation energy in (2) in combination with the coupling term in (3) can be expressed as

$$S(u, \phi) = \int_\Omega H(\phi) d(x + u, M_1)^2 + (1 - H(\phi)) d(x + u, M_2)^2 dx + \alpha |\Gamma| \tag{4}$$

where $H(\phi)$ is the Heaviside function. The constraints of no vacuum and no overlap between the regions are now implicitly entangled into the integral.

A minimization of (4) with respect to u and ϕ attempts to minimize $d(x + u, M_i)^2$ within each segment by two means. First, by dislocating Γ, and second, by moving the grid in u. The latter effect is the segmentation-driven registration. However, it has potentially undesired effects by seeking a maximum likelihood between the training set and the voxel time course at every voxel. This will favour voxels that are highly similar to the training set, and the deformation field will try to expand these regions at the expense of voxels with less similarity. Fairly large deformations far from Γ, in particular volume changes, can thereby occur. A segmentation-driven deformation at a great distance from Γ will not affect the segment association of a voxel, and is therefore undesirable. Our aim with the segmentation-driven registration is to have the largest effects locally around Γ, in order to better distinguish between kidney and non-kidney tissue. Therefore, to promote deformations around Γ, in other words where ϕ is close to zero, we divide by $|\phi|$ in (4). To ensure numerical stability we approximate $|\phi| \approx \sqrt{\phi^2 + \epsilon^2}$, and a new version of (4) becomes

$$S(u, \phi) = \int_\Omega \frac{H(\phi)}{\sqrt{\phi^2 + \epsilon^2}} d(x + u, M_1)^2 + \frac{(1 - H(\phi))}{\sqrt{\phi^2 + \epsilon^2}} d(x + u, M_2)^2 dx + \alpha |\Gamma| \tag{5}$$

for a small $\epsilon > 0$.

C. Boundary Regularization

In line with the literature [47], we consider a regularization on ϕ by the means of a minimization of the total variation $|\nabla \phi|$ of the level set function. We reformulate the boundary regularization as

$$|\Gamma| = \int_\Omega \sqrt{|\nabla \phi|^2 + \epsilon^2} dx. \tag{6}$$

The parameter ϵ is set globally as small as possible to preserve accuracy, and as large as necessary to ensure numerical stability. In our experiments we used the same value of ϵ in (5) and (6). The gradient has been embedded into a convex function to ensure stability for a sufficiently large ϵ and to avoid a singular gradient in the Euler equation for $|\nabla \phi| = 0$. Minimizing the total variation $\sqrt{|\nabla \phi|^2 + \epsilon^2}$ results in mean curvature motion by minimizing the curve length of the level set function.

D. Data and Regularization Terms

The choice of data term $D(u)$ in the cost functional (1) is not trivial. In literature, several data terms have been applied for registration of DCE-MRI time series. Mutual information (MI), or its normalized version (NMI), is the most frequently used data term [27], [37], [48], [52], [56], but also cross correlation [16], [30] and gradient depending cost functionals [38] have been applied. Mutual information is highly nonlinear and also computationally demanding. The wash-in and wash-out is a challenging phenomenon for mutual information where a range of intensities in the input image must match a much smaller intensity range in the target image, thus blurring the joint histogram. The DCE-MRI time series exhibit strong edges upon wash-in and wash-out of bolus, thus registration is intrinsically multi modal within the kidney and mono modal outside. This suggests the use of normalized gradients proposed by Haber and Modersitzki [21]: The cost functional is minimized when the gradients are aligned or co-aligned and is essentially intensity independent. Mathematically, the normalized gradients are defined as

$$\tilde{\nabla} f = \frac{\nabla f}{\sqrt{||\nabla f||^2 + \eta^2}}. \tag{7}$$

The edge parameter η should be tuned in the range of gradients of major image features. The cost functional D for NGF reads

$$D(u) = \int_T \int_\Omega 1 - (\tilde{\nabla} f(x + u, t) \cdot \tilde{\nabla} f_r)^2 dx dt. \tag{8}$$

For the regularization term we choose the linear, elastic regularizer [34]

$$R(u) = \frac{\mu}{4}\sum_{i,j}^{3}\left(\frac{\partial u_j}{\partial x_i} + \frac{\partial u_i}{\partial x_j}\right)^2 + \frac{\lambda}{2}(\nabla \cdot u)^2 \quad (9)$$

with the Lamé constants λ, μ. This choice of $R(u)$ results upon differentiation in the Navier-Lamé equations of elasticity. Thus, the registration process can be regarded as a deforming, compressible continuum.

E. Distance Metric for Segmentation

The distance metric $d(x, M_i)$ represents the similarity of time series between a voxel x and the time series defined by a training set M_i. An intuitive choice of the cost $d(x, M_i)$ used in the segmentation is the squared Euclidean distance in the space spanned by the sampled time points,

$$d^E(x, M_i)^2 = \int_T (f(x,t) - \mu(t; M_i))^2 dt, \quad i = 1, 2, \quad (10)$$

where the average within training set i is given by $\mu : \mathbb{R} \to \mathbb{R}$

$$\mu(t; M_i) = \frac{1}{|M_i|}\int_{M_i} f(y,t)dy. \quad (11)$$

The Euclidean distance is isotropic. Therefore, when a segment consists of a large number of different tissue types with highly varying intensity profiles, we expect the feature space to have a highly anisotropic structure, and thus the Euclidean distance in not well suited.

In order to deal with this problem one can use the more general Mahalanobis distance [29]. This distance is normally stated in a discrete framework measuring the distance between a vector and a matrix representing a n-dimensional (training) set of data $A = [a_{j,k}]_{m\times n}$ with average vector $\tilde{\mu} = [\tilde{\mu}_k]_{n\times 1}$

$$\tilde{\mu}_k := \frac{1}{N}\sum_{j=1}^{N} a_{j,k}.$$

for N voxels in the training mask. For A, the rows are the voxels in the training set, and the columns represent the various time points. The Mahalanobis distance between an arbitrary m-dimensional vector $\tilde{x}$ and the set A is defined as

$$\tilde{d}^M(\tilde{z}, A)^2 = (\tilde{z} - \tilde{\mu})^T \tilde{\Sigma}^{-1}(\tilde{z} - \tilde{\mu}) \quad (12)$$

where $\tilde{\Sigma}$ is the covariance matrix of A, with each element containing the covariance between column i and j in A. $\tilde{\Sigma}$ is therefore symmetric and positive semi-definite. The role of $\tilde{\Sigma}$ is to transform the difference between the feature vector $\tilde{z}$ and $\tilde{\mu}$ to an ellipsoid with principal axes along the eigenvectors of $\tilde{\Sigma}$. Using this transformation, any feature vector $\tilde{z}$ on the ellipsoid has the same distance from the set A, although the Euclidean distance can vary significantly. Note that if $\tilde{\Sigma}$ is the identity, the Mahalanobis distance reduces to the normalized Euclidean distance, while, for $\tilde{\Sigma}$ not the identity, the Mahalanobis distance measure will better reflect the distribution, orientation and variance of the underlying data. When the difference between two feature points is small, the covariance matrix becomes singular and the existence of the inverse is therefore not guaranteed. In this case, the Moore-Penrose pseudoinverse $\tilde{\Sigma}^{-1} \to \tilde{\Sigma}^{+}$, computed by the singular value decomposition of $\tilde{\Sigma}$, is applied instead [19].

The 2D training masks $M_i, i = 1, 2$ in the DCE-MRI data are initialized by the user prior to numerical optimization. These domains are drawn manually in 2D (as a 3D delineation would be a lot more labor intensive) on the reference image f_r. Notably, M_i do not require accurate initiations, but each domain must reflect the amount of various main tissue types that should end up in the corresponding segment after numerical optimization. Define $r(x, t; M_i) := f(x,t) - \mu(t; M_i)$. In a continuous framework the normalized and squared Mahalanobis distance $d^M(x; M_i)^2$ from the time curves of x to the time curves in a training data set defined within M_i can be reformulated as

$$d^M(x; M_i)^2 = \frac{1}{|T|^2}\int_T\int_T r(x,t; M_i)\Sigma^{+}(t,\tau; M_i)r(x,\tau; M_i)d\tau dt \quad (13)$$

where the covariance function $\Sigma : \mathbb{R}^2 \to \mathbb{R}$

$$\Sigma(t,\tau; M_i) = \frac{1}{|M_i|}\int_{M_i} r(x,t; M_i)r(x,\tau; M_i)dx, \quad i = 1, 2$$

has a pseudoinverse Σ^{+} [7]. The discretized version of the pseudoinverse Σ^{+} is the Moore-Penrose pseudoinverse. The normalization constant $|T|^2$ is added to ensure global and consistent parameter settings of β across time series of various extent in time. As an approximation, $\Sigma(t, \tau; M_i)$ and $\mu(t, M_i)$ are not functions of u, since the covariance is assumed to remain almost constant during iterations (cf. Appendix B-C). Combining the registration functional in (1) with the segmentation functional in (4) and by letting $d(x; M_i)^2 \leftarrow d^M(x; M_i)^2$ results in the final normalized Mahalanobis distance driven registration model

$$J^{RegSeg} = \int_T\int_\Omega D(u) + R(u)dxdt\beta\int_\Omega \frac{H(\phi)}{\sqrt{\phi^2+\epsilon^2}}d(x+u, M_1)^2 + \frac{(1-H(\phi))}{\sqrt{\phi^2+\epsilon^2}}d(x+u, M_2)^2dx + \alpha\int_\Omega \sqrt{|\nabla\phi|^2+\epsilon^2}dx. \quad (14)$$

where β is a user-defined weight for the segmentation term. The derivation of the Euler-Lagrange equations for (14) is shown in Appendix A.

III. Numerical Implementation

Numerical issues are not a major focus of this work, and a specific choice of implementation model was applied to demonstrate the usefulness of the model. The domain was discretized as $x_{i,j,k} = (ih_x, jh_y, kh_z)$ for all $i = \{1, \ldots, n_x\}, j = \{1, \ldots, n_y\}, k = \{1, \ldots, n_z\}$ where n_x, n_y, n_z are the number of voxels in the three main coordinate directions. The spatial derivative of a function f was approximated either by central (D_c), forward (D_+) or backward (D_-) differences. The Euler-Lagrange equations to solve are given by (24). Note that $b(u, \phi)$ is not depending on u and ϕ through a differential operator, and is therefore

applied on the right hand side. Upon discretization, the first three elements of (24) are linear in $u_{i,j,k}$ and can be solved by a linear system. However, for easy implementation of Neumann boundary conditions $\partial u_i/\partial x_i = 0$, fixed point iterations (nonlinear Jacobi) were used instead. Each of the discretized components in u were isolated on the left hand side and updated by fixed point iterations in a multigrid framework using FAS (Full Approximation Scheme) [8].

The functional derivative with respect to ϕ can be found as the fourth component of (24) [5], and was solved using an explicit scheme. Introducing an artificial time τ, solving the fourth component of the stationary equation in (24) for ϕ is equivalent to solving the time-dependent PDE

$$\frac{\partial \phi}{\partial \tau} = -\alpha \nabla \cdot \left(\frac{\nabla \phi}{\sqrt{|\nabla \phi| + \epsilon^2}} \right) + b_4 \tag{15}$$

to steady state. A discretization leads to the explicit scheme

$$\phi^{k+1} = \phi^k - \Delta\tau \Bigg[\alpha \Bigg(D_-^x \left(\frac{D_+^x \phi_{i,j,k}^{n+1}}{a_{i,j,k}^n} \right) + D_-^y \left(\frac{D_+^y \phi_{i,j,k}^{n+1}}{a_{i,j,k}^n} \right) + D_-^z \left(\frac{D_+^z \phi_{i,j,k}^{n+1}}{a_{i,j,k}^n} \right) \Bigg) - b_{i,j,k}^{(4)} \Bigg]$$

when defining $a_{i,j,k}^n := \sqrt{|D_c^x \phi_{i,j,k}^n|^2 + \epsilon^2}$. For each fixed point iteration on u, this was solved to steady state using $\Delta\tau = 10^{-4}$. Thus, this becomes a procedure for numerical splitting, sequentially solving for u and ϕ within each fixed point iteration.

IV. Experimental Results

A. Imaging Data

The DCE-MRI recordings were acquired in collaboration with radiologists and MR physicists at the Department of Radiology, Haukeland University Hospital, Bergen. For testing and evaluation of our combined registration and segmentation model, we used ten DCE-MRI datasets acquired on a 1.5 Tesla MR-scanner (Avanto, Siemens). A breath-hold T1-weighted 3D single gradient recall echo (GRE) FLASH3D pulse sequence was used to obtain signal-intensity time curves after administration of a small dose (2 ml) of a Gadolinium-based contrast agent intravenously. For GFR calculations one has to estimate the Gadolinium concentrations [Gd]. They are nonlinearly related to the observed signal intensities, but can be estimated by voxelwise measurements of the pre-contrast relaxation rate R1, since the relation between R1 and [Gd] is linear for low [Gd]. The acquisition parameters for all examinations were TR/TE/FA = 2.41ms/0.87ms/12°, matrix size = 256 × 256, FOV = 425mm, voxelsize = 1.66 × 1.66 × 3mm^3, and number of time points = 55. Dotarem was used as a contrast agent. The participants were healthy, adult volunteers who had given their written consent. In order to have a gold standard for comparison of GFR we also measured the blood clearance of Iohexol for all subjects [6]. The Iohexol measurements were performed several days apart from the MRI measurements due to practical arrangements.

B. Preprocessing of the Images

An affine registration using `FSL's MCFLIRT` [44] was performed prior to elastic registration in order to account for a majority of motion artifacts from strong breathing. In order to keep the inflow artefacts to a minimum, the arterial input function (AIF) was manually selected as a distally placed 2D ROI. The mask for the AIF and the training masks for segmentation were drawn in 2D using `FSL's FSLVIEW` [44]. The same AIF was applied for both left and right kidney within a subject. The manually drawn training masks M_1 and M_2 were created within a few seconds for both kidney and background.

C. Settings

We used the following global parameter settings for all subjects: $\mu = 1, \lambda = 5$ (Lamé constants in the Navier-Lamé operator), $\eta = 0.03$ (edge term in normalized gradients), $\alpha = 1$ (boundary regularization) and $\beta = 10$ (the segmentation weight). Various settings of $\beta = \{1, 5, 10, 20\}$ were explored (not reported for $\beta = 1, 5, 20$) and $\beta = 10$ had the overall best performance among those settings. The Lamé constants were approximated for soft tissue and bone [50]. The number of multilevels in the multigrid was three with a scaling factor of $1/2$ between each level.

D. Evaluation

The experimental part was executed using five different experimental setups:

(a) Unprocessed images.
(b) Affine registration using `FSL's MCFLIRT`.
(c) An initial registration ($\beta = 0$) with NGF as cost functional followed by a plain segmentation ($\beta = 10$) discarding $D(u)$, $R(u)$. This setup represents a traditional, sequential approach for analyzing DCE-MRI images, here referred to as the *Sequential model*.
(d) Our suggested model with combined registration and segmentation, using $\beta = 10$ and NGF as cost function in $D(u)$. This approach is referred to as *RegSeg*.
(e) Only the segmentation functional and the linear elasticity terms, thus excluding $D(u)$ in (14). By this approach we want to demonstrate that the squared Mahalanobis distance in (13) has the potential to act as an independent cost function for co-registration of time series. This setup is referred to as *Seg*, since the only driving force on the deformation field u originates from the segmentation functional.

We use several measures for evaluation of the proposed method: (i) A visual quality check of the segmented tissue. (ii) Kidney volumes for (c), (d) and (e) related to manual segmentation. (iii) Smoothness of time curves. (iv) Sum-of-squared differences (SSD) of a compartment model to the signal intensity curves within the kidney. The latter two criteria have been used in several related publications for evaluation of co-registration of DCE-MRI image time series, and they are in this respect considered as a gold standard for peformance evaluation [2], [22], [30], [33], [48]. The temporal smoothness (iii) as an evaluation criteria is based

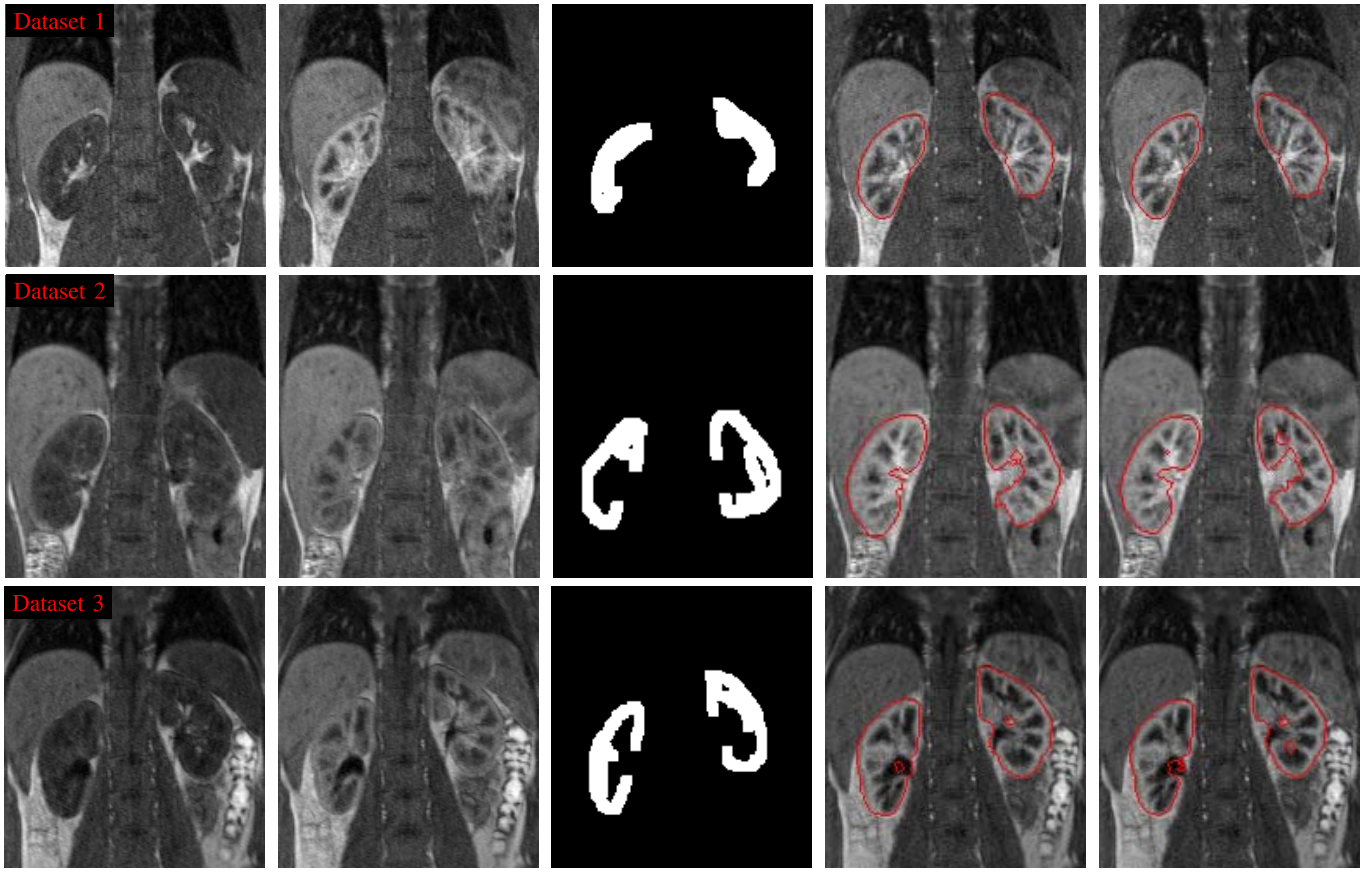

Fig. 3. (Color online) Presentation of images of subjects four, five and six. Left to right: Time instance at pre-, and max-enhancing phase, manually delineated training masks for kidney (background training masks were painted in a lower section), and the overlay of the obtained whole kidney segmentation with the reference image (red, closed curve) using the Sequential and RegSeg model, respectively. Top to bottom: Subjects $1-3$. Both the Sequential model and RegSeg capture the kidney volume, as seen by the red curves in the last two columns. An accurate, manual delineation in 3D is time consuming and demanding with respect to human resources, and is preferably avoided in a clinical perspective. Therefore, the manual initialization is restricted to 2D whereas the final segmentation generates a full 3D volume.

on the assumption that a poor registration is associated with oscillatory time curves. The temporal smoothness of the time curves, here denoted s, was computed by

$$s = \frac{1}{|\Omega||T|}\int_T \int_\Omega \left|\frac{\partial f(x+u,t)}{\partial t}\right| dtdx. \tag{16}$$

For evaluation in (iv) we implemented the two-compartment model in [4] and [46]. Among the five obtained compartment model parameters described in Sourbron et. al [46], we here only report the MR-GFR value (referred to as F_T in [46]). This is because GFR is the only parameter that can be properly validated, as it can be compared with the Iohexol measurements. In the compartment modeling we utilize estimated Gadolinium concentrations based on signal intensity maps of various flip angles for estimation of R1 relaxation rates [12], [45]. The processing time for registration was approximately three hours for a full 4D data set for the Sequential model, and around four hours for RegSeg and Seg.

In order to evaluate the goodnesss of the automatic segmentation we conducted a full kidney segmentation (ii) of both kidneys in all subjects by manual expert delineation (E.E.). The overlap between the manual segmentation and the automated segmentations was measured as described in [23]. For this approach the goodness of segmentation p for a manually segmented ROI R_m and an automatically segmented ROI R_a is expressed as

$$p = \frac{R_m \cap R_a}{R_m \cup R_a}. \tag{17}$$

For a perfect overlap, $p = 1$ and for no overlap $p = 0$.

E. Results

1) The RegSeg Model Provides a 3D Segmentation of the Kidney: The input data for various enhancement regions, the corresponding manual training masks and the segmentations for the Sequential and RegSeg model are visualized in Fig. 3 for three subjects. The segmented kidneys using the Sequential model and RegSeg are outlined by the red, closed curves shown in the second last and last column of Fig. 3, respectively. The combined RegSeg model is able to effectuate a smooth and regularized 3D kidney segmentation for all subjects based on the 2D training masks. A section-wise representation of the 3D segmentation of one data set is shown in Fig. 4 for the proposed RegSeg method. Although the training masks are constructed in 2D the final segmentation is well transferred to 3D. The cost function of RegSeg decreased exponentially with iterations.

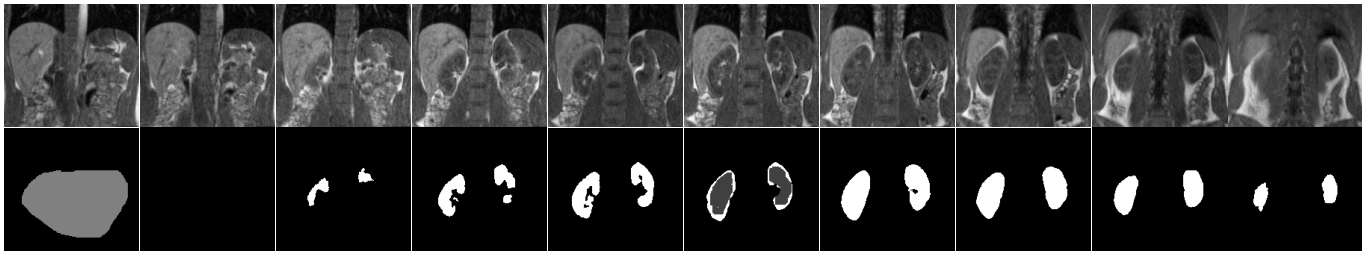

Fig. 4. A 2D planewise visualization of a 3D kidney segmentation of subject one, visualized for every second plane from plane 7 to 26. Upper row: Unprocessed data. Lower row: The 3D segmentation (white) as well as the 2D training masks for kidney and background (gray). The coarse 2D initialization transfers well into a full 3D segmentation.

TABLE I

SEGMENTATION EVALUATION OF THE AUTOMATIC SEGMENTATION VERSUS MANUAL SEGMENTATION. THE SEGMENTATION QUALITY OF THE SEQUENTIAL MODEL, REGSEG, AND SEG IS HERE MEASURED BY p IN (17). THE INTERSECTION OF THE MANUAL AND AUTOMATED SEGMENTATION COVERED BETWEEN 71.9% AND 73.4% OF THE UNION OF AUTOMATED AND MANUAL SEGMENTATION. THE SEQUENTIAL MODEL HAD A SLIGHLTY HIGHER SUCCESS RATE THAN REGSEG AND SEG, BUT THIS DIFFERENCE WAS NOT STATISTICALLY SIGNIFICANT

Data set	Sequential model	RegSeg	Seg
Left, 1	0.731	0.672	0.672
2	0.728	0.758	0.759
3	0.665	0.626	0.625
4	0.809	0.819	0.819
5	0.751	0.717	0.717
6	0.732	0.710	0.710
7	0.845	0.789	0.790
8	0.689	0.698	0.698
9	0.745	0.707	0.707
10	0.682	0.760	0.759
Right, 1	0.686	0.606	0.606
2	0.757	0.776	0.777
3	0.640	0.599	0.597
4	0.698	0.709	0.708
5	0.699	0.656	0.656
6	0.722	0.699	0.699
7	0.791	0.787	0.786
8	0.757	0.774	0.774
9	0.775	0.753	0.752
10	0.776	0.772	0.772
Average	0.734	0.719	0.719

2) The Segmentation Quality of the Sequential Model and RegSeg Is Similar: The whole kidney volumes of the left and right kidney were computed using the Sequential model, RegSeg, Seg, and manual segmentation, and we obtained average volumes of (mean± SE) 163.7 ± 7.2ml,156.9 ± 7.8ml, 156.8 ± 7.8ml and 193.3 ± 8.4ml, respectively. According to the segmentation evaluation term in (17), the segmentation quality of the Sequential model and RegSeg was statistically equal, as reported in Table I (paired t-test, $p = 0.095$).

3) RegSeg Has the Highest Deformation Field: RegSeg has a statistically significantly higher average displacement field (paired t-test, $p < 10^{-3}$). The average displacement fields were 1.971mm, 0.701mm, 0.733mm, and 0.164mm for affine registration, the Sequential model, RegSeg and Seg, respectively.

4) RegSeg Has Smoother Time Curves in All Subjects: The average, temporal variation s of the time curves was estimated by (16) for unprocessed and affine registered data, the Sequential model, RegSeg, and for Seg. There was a statistically significant reduction of temporal variation from the Sequential model to RegSeg, as reported in Table II (paired t-test, $p < 10^{-5}$). The discrepancy of time curves between various registration methods is apparent also visually (c.f. Fig. 5).

TABLE II

AVERAGE TEMPORAL VARIATION s APPLYING (16). REGSEG HAS A STATISTICALLY SIGNIFICANT LOWER TEMPORAL VARIATION COMPARED TO THE SEQUENTIAL MODEL. THIS RESULT IS A STRONG INDICATION OF IMPROVED REGISTRATION ACCURACY OF REGSEG COMPARED TO THE SEQUENTIAL MODEL. NOTE THAT THE MINIMUM TEMPORAL VARIATION IN DCE-MRI WILL NEVER GET CLOSE TO ZERO DUE TO THE USAGE OF A CONTRAST AGENT AND THE PRESENCE OF MR ARTEFACTS AND NOISE

Data set	Unprocessed	Affine	Sequential model	RegSeg	Seg
1	2.89	2.36	2.02	1.99	2.24
2	2.90	2.56	2.28	2.24	2.43
3	2.83	2.37	2.09	2.04	2.25
4	2.75	2.36	2.07	2.05	2.24
5	2.96	2.45	2.11	2.06	2.27
6	2.83	2.33	2.13	2.09	2.35
7	2.86	2.46	2.36	2.33	2.61
8	3.21	2.67	2.78	2.75	3.15
9	2.92	2.41	2.86	2.82	3.17
10	2.68	2.20	2.02	2.01	2.29
Average	2.88	2.42	2.27	2.24	2.50

5) The Compartment Model in RegSeg Has a Better Fit to the Underlying Data: The sum-of-squared differences (SSD) between the observed time curves and the compartment model within each segmented kidney is reported in Table III, showing that RegSeg has on average the lowest SSD, followed by the Sequential model, Seg, affine registration, and unprocessed data in increasing order. The difference between the Sequential model and RegSeg was statistically significant (paired t-test, $p < 10^{-4}$).

6) RegSeg Has a Better Estimation of GFR as Measured by Iohexol Clearance: RegSeg has a smaller MR-GFR deviation to the Iohexol measurements than any of the other methods, as reported int Table IV, although this deviation was not statistical significant (paired t-test, $p = 0.36$).

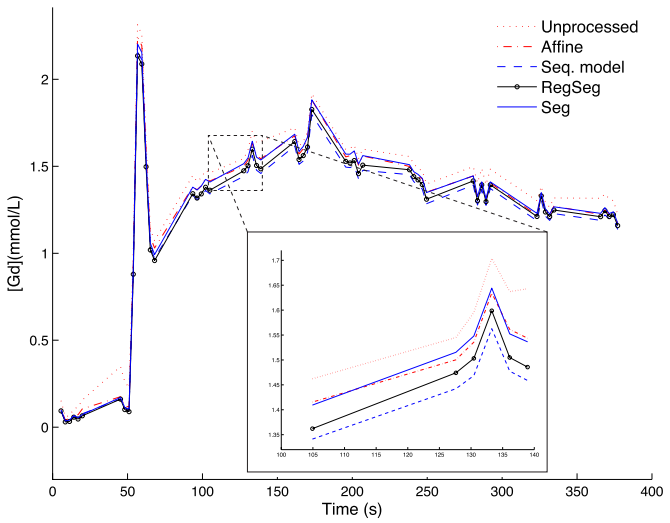

Fig. 5. Average Gadolinium (mmol/L) time curve within left and right kidney for unprocessed data, affine registration, the Sequential model, RegSeg, and Seg in the breath-hold sequence of subject five. Clearly, the curve evolution is depending on the type of registration. The localization and amplitude of the discrepancy are not fixed between subjects and vary significantly (not shown). Sampled time points (o) are linearly interpolated for visualization purposes.

TABLE III

AVERAGE SUM-OF-SQUARED (SSD) DIFFERENCES BETWEEN THE COMPARTMENT MODEL IN [46] AND THE OBSERVED DATA FOR LEFT AND RIGHT KIDNEY. THE DEVIATION BETWEEN THE MODEL AND THE DATA IS ON AVERAGE THE LOWEST FOR REGSEG. SIGNAL INTENSITY VALUES ARE IN [GD]

Data set	Unprocessed	Affine	Sequential model	RegSeg	Seg
Left, 1	0.304	0.267	0.254	0.251	0.261
2	0.322	0.289	0.267	0.264	0.278
3	0.318	0.291	0.283	0.280	0.285
4	0.360	0.376	0.356	0.351	0.371
5	0.296	0.252	0.219	0.213	0.233
6	0.457	0.508	0.483	0.471	0.493
7	0.395	0.366	0.362	0.357	0.387
8	0.286	0.265	0.243	0.240	0.254
9	0.368	0.320	0.315	0.313	0.324
10	0.296	0.272	0.259	0.258	0.269
Right, 1	0.315	0.257	0.243	0.241	0.251
2	0.270	0.245	0.232	0.231	0.238
3	0.306	0.295	0.281	0.278	0.286
4	0.328	0.346	0.326	0.323	0.343
5	0.288	0.247	0.221	0.216	0.232
6	0.387	0.420	0.402	0.392	0.407
7	0.308	0.245	0.239	0.241	0.251
8	0.281	0.226	0.210	0.210	0.238
9	0.387	0.337	0.335	0.332	0.338
10	0.276	0.246	0.233	0.231	0.246
Average	0.327	0.303	0.288	0.285	0.299

V. DISCUSSION

A novel method for segmentation-driven registration of 4D DCE-MRI acquisitions has been introduced in this work. Our method differs from previous work mainly by coupling 4D registration and segmentation into a variational framework, rather than applying sequential iterations of registration and segmentation until convergence. The method does not require an accurate initialization of the segmentation. Instead, a coarse training set is used, from which the Mahalanobis distance to the training masks is computed to guide the actual segmentation problem. Unlike earlier attempts on combined registration/segmentation, our model contains a classical image registration data term and will therefore be driven by spatial information both at the boundaries of the segmented objects, as well as in the rest of the image. The performance of the method has been explored on ten DCE-MRI datasets using the proposed RegSeg model implying 4D registration and 3D segmentation. For all datasets the segmentation of the kidneys performed well visually (cf. Figs. 3–4).

TABLE IV

ESTIMATED GFR (ml/min) FOR THE SUBJECTS INCLUDED IN THE STUDY. THE OBTAINED MR-GFR VALUES WERE COMPARED TO IOHEXOL-GFR, USED AS A GOLD STANDARD. THE AVERAGE, ABSOLUTE DEVIATION TO IOHEXOL-GFR IS REPORTED IN THE LOWER ROW, SHOWING THAT REGSEG HAS THE SMALLEST AVERAGE DEVIATION, ALTHOUGH THIS WAS NOT STATISTICALLY SIGNIFICANT

Data set	Un-processed	Affine	Seq. model	RegSeg	Seg	Iohexol
1	81.2	89.1	93.6	93.5	89.7	128
2	94.7	96.1	99.6	99.1	96.6	97
3	92.5	97.4	100.3	99.3	97.3	104
4	127.7	141.0	129.2	122.8	125.5	124
5	144.0	139.3	136.1	136.1	138.1	91
6	173.8	164.9	153.2	147.1	146.1	128
7	172.6	172.6	172.6	172.6	172.6	103
8	94.1	104.7	99.4	98.7	104.0	109
9	114.2	115.2	121.3	120.7	114.7	135
10	100.9	91.5	89.2	90.0	91.3	89
Average deviation	28.0	24.5	20.9	20.2	20.9	0

We observed a small, but significant increase of the displacement field between RegSeg and the Sequential model. We assume that this increase is due to complementary, time-course related information contained in the segmentation term, which is not fully detected by the edge-sensitive normalized gradient fields. Moreover, Seg had by far the lowest deformation field. This is due to lack of a traditional data term, but can also be accounted for by the lack of a target image. The image time series are therefore free to align at the overall minimum deformation field.

The average segmentation quality was between 71.9–73.4% for the Sequential model, RegSeg and Seg in the comparison to manual segmentation (cf. Table I). This is a high success rate in light of the results from repeated renal segmentation reported in Giovanni Di Leo et al. [26], where it was demonstrated an intraobserver reproducibility at 95% and interobserver variability of 87–88% between manual observers. For most of our subjects, RegSeg resulted in slightly lower kidney volume. The reason for this reduction is unclear, but it can originate from a stronger regularization effect compared to the Sequential model. On the other hand, statistically there was no difference between the Sequential model and RegSeg in terms of segmentation accuracy. A larger sample is needed in order to make firm conclusions about possible effects of RegSeg on kidney segmentation, and based on the current data we can not claim that RegSeg provided an improved segmentation. However, there exist

numerous highly specialized methods for two- or multi-region segmentation, which could most likely provide an improved segmentation of the kidney compared to our approach. Therefore, we claim that the RegSeg approach is basically optimized to improve the registration time-courses and not targeted on the task of optimized segmentation. A separate and highly accurate segmentation procedure based on specialized algorithms for kidney segmentation could be applied after the completion of RegSeg.

We also observed smoother time curves for RegSeg (cf. Table II), and the average deviation between a compartment model and the measured data was the smallest for RegSeg (cf. Table III). These two observations indicate that RegSeg has better performance than the Sequential model by feeding dynamic time-coarse information into the registration machinery and thereby creating smoother time curves.

For the MR-GFR measurements we obtained the smallest deviance to Iohexol using RegSeg, where the average deviance was in the order of 20%. These results are fairly good in light of results from repeated investigations of Iohexol-measured GFR in subjects with normal renal function, where the total variation was shown to be around 11% [13]. Most of this variation is probably due to biological variation, e.g. due to sampling at different time points. Thus, a significant portion of our observed deviance between Iohexol-GFR and MR-GFR can be accounted for by an actual change in renal filtration. Another significant source of deviation in the GFR measurements is probably inflow artifacts of the AIF [45], reflecting image acquisition quality and thus is unrelated to the segmentation/registration problem.

Traditionally, the registration of DCE-MRI time series is separated from anatomical image segmentation. Some studies, however, have reported a registration procedure that incorporates a temporal smoothness constraint on the obtained time curves. This has been accomplished in terms of a least squares fitting of the recorded time courses to a parameterized solution of a pharmacokinetic multi-compartment model [2], [9], [22]. Our model is related to those studies by introducing another data term into the registration, sensitive to temporal dynamics. However, instead of using a criterion of small deviation between data and model, our registration is driven by the criterion of consistent segmentation according to a segmentation model. In the context of the ill-posed registration problem, the use of such penalizing term can guide the registration process towards an admissible displacement field that is anatomically plausible. We claim that this process is driven by anatomical features and physiological properties since voxels of similar tissue have the highest temporal similarity in response to the contrast agent. This assumption is reasonable since similar tissue also has similar function, physiological role, anatomical structure and metabolism, which can be the reason for the observed improvements in RegSeg compared to the Sequential model.

An interesting feature about our RegSeg model is the possibility to integrate a model-driven registration algorithm within the renal compartments [2], [9], [22]. By such construct, a comprehensive and deformable 'RegSegFilt' model could be obtained, where the registration, segmentation and pharmacokinetic compartment model for the glomerular filtration is imbedded into one optimization algorithm. Such approach will likely be less prone to errors due to internal feedback control mechanisms between the various components of the algorithm, compared to the sequential registration-segmentation-pharmacokinetics steps that are normally conducted.

VI. Conclusion

We have presented a novel method for combined registration and segmentation, applicable to 4D DCE-MRI acquisitions of the moving human kidney. The segmentation term affects the registration by enforcing time course similarity of voxels inside and outside the kidney. Using time series data from ten different DCE-MRI examinations we have demonstrated plausible and promising results, in particular related to the smoothness of the voxel time courses and small deviance to Iohexol-measured GFR. We conclude that our segmentation-driven registration approach has a great potential for further development into a full-blown pharmacokinetic GFR model-driven segmentation of the kidneys.

Appendix A
The Euler-Lagrange Equations

Define the cost functional

$$J(u,\phi) = \int_\Omega d(x+u, M_1)^2 dx, \tag{18}$$

consisting of the first segmentation term in (14), and where we have omitted the Heaviside depending factor which is constant in u, and can therefore be added after differentiation. According to (13), the time-normalized Mahalanobis distance to training set one reads

$$d(x; M_1)^2 = \frac{1}{T^2}\int_T\int_T r_1(x,t) S^{-1}(t,\tau) r_1(x,\tau) d\tau dt \tag{19}$$

for $r_1(x,t) := r(x,t;M_1) = f(x,t) - \mu(t;M_1)$ and $S_1^{-1}(t,\tau) := S^{-1}(t,\tau;M_1)$. For brevity, denote $X = x+u$. In the following, we assume that $\mu(t;M_i)$ and $S^{-1}(t,\tau;M_i)$ have no variation with u, which is an approximation (c.f. Appendices B and C). The first variation of (18) with respect to $u = u(x,t)$ becomes

$$\begin{aligned}
\delta J &= \frac{1}{T^2}\int_\Omega\int_T\int_T \Big(r_1(X,\tau) S_1^{-1}(t,\tau) \nabla f(X,t)\cdot \delta u(x,t) \\
&\quad + r_1(X,t) S_1^{-1}(t,\tau)\nabla f(X,\tau)\cdot \delta u(x,\tau)\Big) d\tau dt dx \\
&= \frac{1}{T^2}\int_T\int_\Omega \Big(\int_T r_1(X,\tau) S_1^{-1} \nabla f(X,t) d\tau\Big)\cdot \delta u(x,t) dx dt \\
&\quad + \frac{1}{T^2}\int_T\int_\Omega \Big(\int_T r_1(X,t) S_1^{-1}\nabla f(X,\tau) dt\Big)\cdot \delta u(x,\tau) dx d\tau \\
&= \int_T\int_\Omega h(x+u,t;M_1)\cdot \delta u(x,t) dx dt
\end{aligned} \tag{20}$$

given

$$h(x+u,t;M_1) = \frac{2}{T^2}\int_T r_1(x+u,\tau) S_1^{-1}(t,\tau)\nabla f(x+u,t) d\tau$$

and where we have used the symmetry property $S^{-1}(t,\tau) = S^{-1}(\tau,t)$. The fundamental theorem of calculus of variations

results in the Euler-Lagrange equations of (18) from arbitrary variation of $\delta u(x,t)$ over Ω and T as

$$h(x+u,t;M_1)=0. \tag{21}$$

A corresponding expression can be found for the second segmentation term related to $d(x,M_2)^2$, thus providing $h(x+u,t;M_2)=0$. Recall D as the data term in (1) for registration such that $\delta D/\delta u$ becomes its functional derivative. The functional derivative of (14) with respect to u then becomes

$$b_u(x+u,t,\phi) := \frac{\delta D}{\delta u} + \beta\Bigg(\frac{H(\phi)}{\sqrt{\phi^2+\epsilon^2}}h_1(x+u,t) + \frac{(1-H(\phi))}{\sqrt{\phi^2+\epsilon^2}}h_2(x+u,t)\Bigg) \tag{22}$$

for the three components of u and when not considering the regularization term $R(u)$ in (14). The derivative of (14) with respect to ϕ becomes

$$b_\phi(x+u,t,\phi) := \frac{\beta}{(\phi^2+\epsilon^2)^{3/2}}\Big((\delta(\phi)(\phi^2+\epsilon^2)-\phi H(\phi))d_1(x+u)^2 - (\delta(\phi)(\phi^2+\epsilon^2)+\phi(1-H(\phi)))d_2(x+u)^2\Big) \tag{23}$$

when omitting $|\nabla\phi|$. In (23), we have used the relation $\delta(\phi)=H'(\phi)$. The first variation of $|\nabla\phi|$ is the mean curvature and can be found in [11]. The functional derivative of the regularization terms with respect to u becomes the Navier-Lamé operator [34], thus ending up with the following Euler-Lagrange equations to solve,

$$\begin{bmatrix}\mu\Delta u+(\lambda+\mu)\nabla(\nabla\cdot u)\\ \alpha\nabla\cdot\left(\frac{\nabla\phi}{\sqrt{|\nabla\phi|^2+\epsilon^2}}\right)\end{bmatrix}=\begin{bmatrix}b_u(x+u,t,\phi)\\ b_\phi(x+u,t,\phi)\end{bmatrix}. \tag{24}$$

From top to bottom, the operators on the left hand side of the equation are the Navier-Lamé operator and the mean curvature, respectively.

Appendix B
First Variation of $\mu(t,u;M_i)$

Assume that μ is a function of u. Then

$$\mu(u,t;M_i) := \frac{1}{|M_i|}\int_{M_i} f(y+u(y,t),t)dy \tag{25}$$

where y is a spatial integration variable within the training mask M_i. The first variation of μ with respect to u becomes

$$\delta\mu(u,t;M_i)=\frac{1}{|M_i|}\int_{M_i}\nabla f(y+u(y,t),t)\cdot\delta u(y,t)dy \tag{26}$$

which would be added to the $\nabla f(X,\cdot)$ terms in the first equality sign of (20) if μ depends on u. For the next we make the following assumptions: (i) The image f is approximately homogeneously distributed in a neighbourhood $u_{\max}$ around the boundary of the training mask ∂M_i, where $u_{\max}=\max_{\partial M_i}|u|$ is the maximum deformation field on ∂M_i. (ii) The training mask M_i is entirely within Ω, $M_i\subset\Omega$. (iii) Image values f are finite. Equation (26) can be thought of as the directional derivative $\partial f/\partial l$, where l is a unit length along the direction of δu. Any change of (26) due to variations in u would mainly be caused by deformations across ∂M_i. Therefore, due to assumptions (i)–(iii), the integral (26) will be close zero. Assumption (ii) is needed in order to avoid out of range values of f close to the image boundaries. These could, if they for instance were set to zero, represent a systematic change of f on ∂M_i. Hence, $\delta\mu$ can be considered constant in u and the first variation of r_i can be approximated as $\delta r(x,t;M_i)=\nabla f\cdot\delta u$, which is used in Appendix A.

Appendix C
First Variation of Σ^{-1}

Now, we consider the discretized covariance matrix $\tilde{\Sigma}$, originating from the covariance between the columns of the training data matrix F associated with Ω_i. Taking the differential of $\tilde{\Sigma}^{-1}\tilde{\Sigma}=I$ provides the differential formula for the inverse

$$\delta(\tilde{\Sigma}^{-1})=-\tilde{\Sigma}^{-1}\delta\tilde{\Sigma}\,\tilde{\Sigma}^{-1},\quad i=1,2. \tag{27}$$

If $\delta\tilde{\Sigma}\to 0$ then $\delta\tilde{\Sigma}^{-1}\to 0$ assuming the elements of $\tilde{\Sigma}^{-1}$ are finite, which is true for non-constant data in time. From this observation we only need to investigate the behavior of $\delta\tilde{\Sigma}$. With N as the number of rows (corresponding to the number of voxels in M_i) in the training set matrix F, the covariance matrix $\tilde{\Sigma}$ can be expressed as a matrix product

$$\tilde{\Sigma}=\frac{1}{N-1}F^TF, \tag{28}$$

where each column of a training data matrix F contains spatial image data from a selected time point within the training mask defined by M_i, and where the columns of F have zero mean after subtraction of the column mean. Subtraction of the column mean $\tilde{\mu}_j$ from column j of F for $j=1,\ldots,t_n$ prior to differentiation is justified since the continuous counterpart of $\tilde{\mu}$ was in the previous section shown to be essentially independent of u and can therefore be considered a constant for subtraction. The differential of $\tilde{\Sigma}$ becomes

$$\delta\tilde{\Sigma}=\frac{1}{N-1}\delta(F^TF)=\frac{1}{N-1}\Big((\delta F^T)F+F^T(\delta F)\Big). \tag{29}$$

Denote the training set data

$$F=\begin{bmatrix}\tilde{f}_{1,1} & \tilde{f}_{1,2} & \cdots\\ \tilde{f}_{2,1} & \tilde{f}_{2,2} & \cdots\\ \tilde{f}_{3,1} & \tilde{f}_{3,2} & \cdots\\ \vdots & & \ddots\end{bmatrix} \tag{30}$$

where $\tilde{f}_{k,l}$ indicates discretized values of f for voxel k and time l after subtracting the column mean. The first variation δF^T in (29) becomes a matrix of dot products

$$\delta F^T=\begin{bmatrix}\nabla\tilde{f}_{1,1}\cdot\delta\tilde{u}_{1,1} & \nabla\tilde{f}_{2,1}\cdot\delta\tilde{u}_{2,1} & \nabla\tilde{f}_{3,1}\cdot\delta\tilde{u}_{3,1} & \cdots\\ \nabla\tilde{f}_{1,2}\cdot\delta\tilde{u}_{1,2} & \nabla\tilde{f}_{2,2}\cdot\delta\tilde{u}_{2,2} & \nabla\tilde{f}_{3,2}\cdot\delta\tilde{u}_{3,2} & \cdots\\ \vdots & & & \ddots\end{bmatrix}. \tag{31}$$

where $\tilde{u}_{k,l}$ is the discretised deformation field vector for voxel k and time point l. When multiplying with F we get a new matrix where each element becomes a sum $\sum_{k=1}^{n} \tilde{f}_{k,j} \nabla \tilde{f}_{k,i} \cdot \delta\tilde{u}_{k,i}$. The second additive term in (29) will be equal due to symmetry. This sum can in a continuous setting be phrased as

$$\int_{M_i} (f \nabla f \cdot \delta u(y,t)) dy = \frac{1}{2} \int_{M_i} (\nabla (f^2) \cdot \delta u(y,t)) dy,$$

which means that f^2 needs to be approximately constant on the boundaries of M_i, following from assumptions (i)–(iii) and the discussion in the previous section. For practical registration tasks, we always scale the image f between zero and one, so the difference between homogeneous distribution of f versus f^2 is small. Hence, $\tilde{\Sigma}^{-1}$ can be considered independent of u in the calculation of the first variation without substantial loss of accuracy.

ACKNOWLEDGMENT

The authors want to thank Jarle Rørvik at Department of Radiology, University of Bergen, for providing the DCE-MRI data.

REFERENCES

[1] H. Abdelmunim, A. Farag, W. Miller, and M. AboelGhar, "A kidney segmentation approach from DCE-MRI using level sets," in *Proc. IEEE Comput. Soc. Conf. CVPRW*, Jun. 2008, pp. 1–6.

[2] G. Adluru, E. V. DiBella, and M. C. Schabel, "Model-based registration for dynamic cardiac perfusion MRI," *J. Magn. Reson. Imag.*, vol. 24, no. 5, pp. 1062–1070, Nov. 2006.

[3] A. M. Ali, A. A. Farag, and A. S. El-Baz, "Graph cuts framework for kidney segmentation with prior shape constraints," in *Proc. MICCAI*, vol. 10. 2007, pp. 384–392.

[4] L. Annet, L. Hermoye, F. Peeters, F. Jamar, J.-P. Dehoux, and B. E. V. Beers, "Glomerular filtration rate: Assessment with dynamic contrast-enhanced MRI and a cortical-compartment model in the rabbit kidney," *J. Magn. Reson. Imag.*, vol. 20, no. 5, pp. 843–849, Nov. 2004.

[5] G. Aubert and L. Vese, "A variational method in image recovery," *SIAM J. Numer. Anal.*, vol. 34, no. 5, pp. 1948–1979, 1997.

[6] N. J. Bird, C. Peters, A. R. Michell, and A. M. Peters, "Reproducibilities and responses to food intake of GFR measured with chromium-51-EDTA and iohexol simultaneously and independently in normal subjects," *Nephrol. Dial. Transplant.*, vol. 23, pp. 1902–1909, May 2008.

[7] A. Böttcher, "C*-algebras in numerical analysis," *Irish Math. Soc. Bullet.*, vol. 45, pp. 57–133, Dec. 2000.

[8] W. L. Briggs, V. E. Henson, and S. F. McCormick, *A Multigrid Tutorial*. Philadelphia, PA, USA: SIAM, 2000.

[9] G. A. Buonaccorsi *et al.*, "Tracer kinetic model-driven registration for dynamic contrast-enhanced MRI time-series data," *Magn. Reson. Med.*, vol. 58, no. 5, pp. 1010–1019, 2007.

[10] T. F. Chan and L. Vese, "Active contours without edges," *IEEE Trans. Image Process.*, vol. 10, no. 2, pp. 266–277, Feb. 2001.

[11] T. F. Chan and J. Shen, *Image Processing and Analysis: Variational, PDE, Wavelet, and Stochastic Methods*. Philadelphia, PA, USA: SIAM, 2005.

[12] H.-L. M. Cheng and G. A. Wright, "Rapid high-resolution T_1 mapping by variable flip angles: Accurate and precise measurements in the presence of radiofrequency field inhomogeneity," *Magn. Reson. Med.*, vol. 55, no. 3, pp. 566–574, 2006.

[13] E. Krutzén, S. E. Bäck, I. Nilsson-Ehle, and P. Nilsson-Ehle, "Plasma clearance of a new contrast agent, iohexol: A method for the assessment of glomerular filtration rate," *J. Lab Clin. Med.*, vol. 104, no. 6, pp. 955–961, 1984.

[14] E. Hodneland, A. Lundervold, J. Rørvik, and A. Z. Munthe-Kaas, "Normalized gradient fields and mutual information for motion correction of DCE-MRI images," in *Proc. 8th Int. Symp. Image Signal Process.*, 2013, pp. 516–521.

[15] J. Ehrhardt, A. Schmidt-Richberg, and H. Handels, "A variational approach for combined segmentation and estimation of respiratory motion in temporal image sequences," in *Proc. IEEE 11th ICCV*, Oct. 2007, pp. 1–7.

[16] A. El-Baz, A. Farag, R. Fahmi, S. Yuksela, M. A. El-Ghar, and T. Eldiasty, "Image analysis of renal DCE-MRI for the detection of acute renal rejection," in *Proc. 18th ICPR*, vol. 3. 2006, pp. 822–825.

[17] K. Ens, J. Berg, and B. Fischer, "A communication term for the combined registration and segmentation," in *Proc. 4th Eur. Conf. IFMBE*, vol. 22. 2009, pp. 673–675.

[18] B. Fischer and J. Modersitzki, "III-posed medicine—An introduction to image registration," *Inverse Problems*, vol. 24, no. 3, pp. 1–16, May 2008.

[19] G. H. Golub and C. F. V. Loan, *Matrix Computations*. Baltimore, MD, USA: The Johns Hopkins Univ. Press, 1996.

[20] C. L. Guyader and L. A. Vese, "A combined segmentation and registration framework with a nonlinear elasticity smoother," *Comput. Vis. Image Understand.*, vol. 115, no. 12, pp. 1689–1709, 2011.

[21] E. Haber and J. Modersitzki, "Intensity gradient based registration and fusion of multi-modal images," in *Medical Image Computing and Computer-Assisted Intervention* (Lecture Notes in Computer Science), vol. 4191. Berlin, Germany: Springer-Verlag, 2006, pp. 726–733.

[22] P. Hayton, M. Brady, L. Tarassenko, and N. Moore, "Analysis of dynamic MR breast images using a model of contrast enhancement," *Med. Image Anal.*, vol. 1, no. 3, pp. 207–224, 1997.

[23] E. Hodneland *et al.*, "A unified framework for automated 3D segmentation of surface-stained living cells and a comprehensive segmentation evaluation," *IEEE Trans. Med. Imag.*, vol. 28, no. 5, pp. 720–738, May 2009.

[24] E. Hodneland, A. Lundervold, J. Rørvik, and A. Z. Munthe-Kaas, "Normalized gradient fields for nonlinear motion correction of DCE-MRI time series," *Comput. Med. Imag. Graph.*, vol. 38, no. 3, pp. 202–210, Apr. 2014.

[25] E. Hodneland *et al.*, "In vivo estimation of glomerular filtration in the kidney using DCE-MRI," in *Proc. 7th Int. Symp. ISPA*, 2011, pp. 755–761.

[26] G. D. Leo, F. D. Terlizzi, N. Flor, A. Morganti, and F. Sardanelli, "Measurement of renal volume using respiratory-gated MRI in subjects without known kidney disease: Intraobserver, interobserver, and interstudy reproducibility," *Eur. J. Radiol.*, vol. 80, no. 3, pp. 212–216, 2011.

[27] X. Li *et al.*, "A nonrigid registration algorithm for longitudinal breast MR images and the analysis of breast tumor response," *Magn. Reson. Imag.*, vol. 27, no. 9, pp. 1258–1270, Nov. 2009.

[28] F. Maes, A. Collignon, D. Vandermeulen, G. Marchal, and P. Suetens, "Multimodality image registration by maximization of mutual information," *IEEE Trans. Med. Imag.*, vol. 16, no. 2, pp. 187–198, Apr. 1997.

[29] P. C. Mahalanobis, "On the generalised distance in statistics," in *Proc. Nat. Inst. Sci. India*, vol. 2. 1936, pp. 49–55.

[30] A. Melbourne, D. Atkinson, M. J. White, D. Collins, M. Leach, and D. Hawkes, "Registration of dynamic contrast-enhanced MRI using a progressive principal component registration (PPCR)," *Phys. Med. Biol.*, vol. 52, no. 17, pp. 5147–5156, 2007.

[31] I. Mendichovszky *et al.*, "How accurate is dynamic contrast-enhanced MRI in the assessment of renal glomerular filtration rate? A critical appraisal," *J. Magn. Reson. Imag.*, vol. 27, no. 4, pp. 925–931, Apr. 2008.

[32] N. Michoux *et al.*, "Analysis of contrast-enhanced MR images to assess renal function," *Magma*, vol. 19, no. 4, pp. 167–179, Sep. 2006.

[33] J. Milles, R. J. van der Geest, M. Jerosch-Herold, J. H. Reiber, and B. P. Lelieveldt, "Fully automated motion correction in first-pass myocardial perfusion MR image sequences," *IEEE Trans. Med. Imag.*, vol. 27, no. 11, pp. 1611–1621, Nov. 2008.

[34] J. Modersitzki, *Numerical Methods for Image Registration*. Oxford, U.K.: Oxford Science, 2004.

[35] J. Modersitzki, *FAIR: Flexible Algorithms for Image Registration*. Philadelphia, PA, USA: SIAM, 2009.

[36] S. Parisot, H. Duffau, S. Chemouny, and N. Paragios, "Joint tumor segmentation and dense deformable registration of brain MR images," in *Proc. 15th Int. Conf. MICCAI*, vol. 2. 2012, pp. 651–658.

[37] K. Passera *et al.*, "A non-linear registration method for DCE-MRI and DCE-CT comparison in bladder tumors," in *Proc. 5th IEEE ISBI Nano Macro*, May 2008, pp. 1095–1098.

[38] J. P. Pluim, J. B. Maintz, and M. A. Viergever, "Image registration by maximization of combined mutual information and gradient information," *IEEE Trans. Med. Imag.*, vol. 19, no. 8, pp. 809–814, Aug. 2000.

[39] R. B. Potts, "Some generalized order-disorder transformations," Ph.D. dissertation, Math. Proc. Cambridge Phil. Soc., Cambridge, U.K., 1952.
[40] L. Ruthotto, E. Hodneland, and J. Modersitzki, "Registration of dynamic contrast enhanced MRI with local rigidity constraint," in *Proc. 5th WBIR*, 2012, pp. 190–198.
[41] S. Johnson *et al.*, "Determinants and functional significance of renal parenchymal volume in adults," *Clin. J. Amer. Soc. Nephrol.*, vol. 6, no. 1, pp. 70–76, 2011.
[42] P. Shah and M. D. Gupta, "Simultaneous registration and segmentation by l1 minimization," in *Machine Learning in Medical Imaging* (Lecture Notes in Computer Science), vol. 7588, F. Wang, D. Shen, P. Yan, and K. Suzuki, Eds. Berlin, Germany: Springer-Verlag, 2012, pp. 128–135.
[43] D. Shen and C. Davatzikos, "Measuring temporal morphological changes robustly in brain MR images via 4-dimensional template warping," *Neuroimage*, vol. 21, no. 4, pp. 1508–1517, 2004.
[44] S. M. Smith *et al.*, "Advances in functional and structural MR image analysis and implementation as FSL," *Neuroimage*, vol. 23, no. 1, pp. S208–S219, 2004.
[45] S. Sourbron, "Technical aspects of MR perfusion," *Eur. J. Radiol.*, vol. 76, no. 3, pp. 304–313, Dec. 2010.
[46] S. P. Sourbron, H. J. Michaely, M. F. Reiser, and S. O. Schoenberg, "MRI-measurement of perfusion and glomerular filtration in the human kidney with a separable compartment model," *Invest Radiol.*, vol. 43, no. 1, pp. 40–48, 2008.
[47] X.-C. Tai and T. F. Chan, "A survey on multiple set methods with applications for identifying piecewise constant functions," *Int. J. Numer. Anal. Model.*, vol. 1, no. 1, pp. 25–48, 2004.
[48] J. Tokuda *et al.*, "Impact of nonrigid motion correction technique on pixel-wise pharmacokinetic analysis of free-breathing pulmonary dynamic contrast-enhanced MR imaging," *J. Magn. Reson. Imag.*, vol. 33, no. 4, pp. 968–973, Apr. 2011.
[49] P. Viola and W. M. Wells, "Alignment by maximization of mutual information," *Int. J. Comput. Vis.*, vol. 24, no. 2, pp. 137–154, 1997.
[50] Z. Wang and J. C. Lin, "Thermoelastic pressure waves induced inside the human head by RF pulses from high pass birdcage coils," in *Proc. Int. Soc. Magn. Reson. Med.*, 2006.
[51] A. Yezzi, L. Zöllei, and T. Kapur, "A variational framework for integrating segmentation and registration through active contours," *Med. Image Anal.*, vol. 7, no. 2, pp. 171–185, 2003.
[52] C. Zakkaroff, D. Magee1, A. Radjenovic, and R. Boyle1, "Mediated spatiotemporal fusion of multiple cardiac magnetic resonance datasets for patient-specific perfusion analysis," in *Proc. Comput. Cardiol.*, vol. 37. 2010, pp. 469–472.
[53] J. L. Zhang, H. Rusinek, H. Chandarana, and V. S. Lee, "Functional MRI of the kidneys," *J. Magn. Reson. Imag.*, vol. 37, no. 2, pp. 282–293, 2013.
[54] S. T. Wong, Z. Xue, and K. Wong, "Joint registration and segmentation of serial lung CT images for image-guided lung cancer diagnosis and therapy," *Comput. Med. Imag. Graph.*, vol. 34, no. 1, pp. 55–60, 2010.
[55] D. Zikic, S. Sourbron, X. Feng, H. J. Michaely, A. Khamene, and N. Navab, "Automatic alignment of renal DCE-MRI image series for improvement of quantitative tracer kinetic studies," *Proc. SPIE*, vol. 6914, pp. 691432–691440, Feb. 2008.
[56] F. G. Zöllner *et al.*, "Assessment of 3D DCE-MRI of the kidneys using non-rigid image registration and segmentation of voxel time courses," *Comput. Med. Imag. Graph.*, vol. 33, no. 3, pp. 171–181, Apr. 2009.
[57] F. G. Zöllner, E. Svarstad, A. Z. Munthe-Kaas, L. R. Schad, A. Lundervold, and J. Rørvik, "Assessment of kidney volumes from MRI: Acquisition and segmentation techniques," *AJR Amer. J. Roentgenol.*, vol. 199, no. 5, pp. 1060–1069, Nov. 2012.

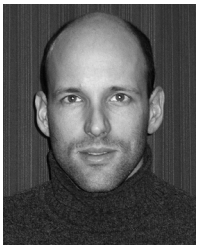

Erlend Hodneland received the M.Sc. degree in applied mathematics and the Ph.D. degree in medical image processing from the University of Bergen (UoB), Norway, in 2003 and 2009, respectively. He is currently a Post-Doctor with the Department of Biomedicine, UoB, and affiliated with the Neuroinformatics and Image Analysis Laboratory. During the Ph.D. degree, his main project was to develop algorithms for 3-D automated segmentation of fluorescently labeled cells. His current research interests are within applied image processing with focus on image registration and motion compensation of multimodal MR images and MRI perfusion time series.

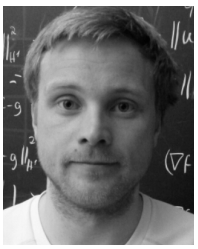

Erik A. Hanson received the B.Sc. degree in mathematics and the M.Sc. degree in applied mathematics from the University of Bergen (UoB), Norway, in 2008 and 2010, respectively, where he is currently pursuing the Ph.D. degree with the Department of Mathematics. He is doing research on mathematical image processing with applications to medical imaging data. His main focus is on spatiotemporal segmentation and registration of MRI. He is affiliated to the Neuroinformatics and Image Analysis Laboratory, Department of Biomedicine, UoB, and the MedViz research cluster.

Arvid Lundervold received the B.Sc. and M.D. degrees from the University of Oslo, Norway, and the Ph.D. degree in medical image analysis from the University of Bergen, Norway. He is currently a Professor of Medical Information Technology with the University of Bergen, and the Head of the Neuroinformatics and Image Analysis Laboratory, Neural Networks Research Group. His research interests are in the fields of image processing and pattern recognition, functional imaging, image registration, quantification and visualization, and mathematical modeling. He is a member of the IEEE Computer Society.

Jan Modersitzki received the Diploma degree and the Ph.D. degree in Mathematics from the University of Hamburg, Germany, in 1990 and 1995, respectively. In 1995, he joined the Institute of Mathematics, (Medical) University of Lübeck, Germany, where he was involved in medical imaging problems, in particular, correspondence and registration problems. His habilitation thesis appeared as one of the first monographs on this timely topic in 2003. In 2003, he spend one year as a Visiting Assistant Professor with the Emory University, Atlanta, bridging the medical and the mathematics and computer sciences schools. From 2008 to 2009, he was an Associate Professor with the Department of Computing and Software, McMaster University, Hamilton, Canada. Since 2010, he has been a Professor with the Institute of Mathematics and Image Computing, University of Lübeck, and a member of the Fraunhofer MEVIS Project Group Image Registration. His interest is in mathematical and biomedical imaging, numerical analysis, numerical optimization, optimization, partial differential equations, and the calculus of variations.

Eli Eikefjord received the B.Sc. degree in radiography from the Bergen University College and the M.Sc. degree in health sciences from the University of Bergen in 2001 and 2005, respectively. She is currently pursuing the Ph.D. degree in medicine with the Department of Radiology, Haukeland University Hospital, University of Bergen. Her current research topic includes functional renal MRI focusing on optimization and quality assessment of acquisition techniques and clinical implementation.

Antonella Z. Munthe-Kaas received the Ph.D. degree from the University of Cambridge, U.K. She is a Professor of Applied and Computational Mathematics with the University of Bergen, Norway. Her main focus of research is numerical methods for differential equations. She has an interest in medical image analysis and processing, and has been a Steering Board Member of the MedViz research cluster for several years. In this field, her research interests are image registration and modeling of kidney function.